Abstract

Chapter 1

Introduction

1.1 Introduction

Resonant Ultrasound Spectroscopy (RUS) is a measurement technique for material properties of an elastic object that uses resonant frequencies of the material. Resonant frequencies are usually obtained through a very simple experiment using two or more ultrasonic transducers. For anisotropic materials, it is capable of extracting all 21 elastic constants. Exciting the object and recording the responses are the two major parts of the experiment. The main advantage of RUS is the simplicity of the experiment. Theoretically, the vibration spectrum of an elastic object contains much information about the object, both microscopic and macroscopic. Thermodynamic properties e.g. entropy and Helmholz free energy can also be measured using RUS [25] [1].

Obtaining the elastic constants from the spectrum is usually referred as the "inverse problem" in RUS. The "forward problem" is the solution of the mathematical model which depends on the shape of the object. This means that a numerical approximation is used to predict the resonant spectrum of the object, and this approximation is compared to the measured spectrum. If the measured and calculated spectrum do not agree within the acceptable limits, the parameters used in the calculation are adjusted and the computation is redone until the error reaches to a tolerable limit. This iterative process is the basis of the RUS method. Initially the RUS method was limited to particular types of shapes, with high symmetry such as cylinders, spheres, and rectangular parallelepipeds (RP) [17].

But more recently attempts have been made to study arbitrarily shaped objects by Maynard [18]. Study of carbon nanotubes was the first attempt to study the hollow geometry [16].

1.1.1 History

It was known before the industrial revolution that sound carries information of the vibrating object. Before any scientific development, bell makers around the world knew that different alloys produce different sound, and the shape of the object is important in the quality of the sound. This is an early example how shape and material influence the sound quality. Presence of any kind of crack or imperfection changes the sound quality. Knowledge of the relationship between shape, material, and resonant frequency was used in a variety of fields. Before World War I, British railroad engineers had a similar type of technique. They would tap the wheels of the train and use the sound to detect cracks. This may be the first engineering use of sound to test material performance [24]. Later attempts were made to understand the resonance of solids mathematically based on the shape and composition. Nobel laureate Lord Rayleigh's contribution in the late eighteenth century was significant. In World War II German engineers utilized a violinist to rub his bow over different turbine blade designs to verify that the resonant frequencies of the blades would be very different from the angular speed of the engine itself to avoid the catastrophic failure that could result from the resonant frequency of the blade [10]. The knowledge of natural resonance is also important in structure design.

Interest in elastic properties goes back to the 17th century when Galileo and other philosophers studied the static equilibrium of bending beams. In 1660 Robert Hooke first developed the law of elasticity. With the help of mathematicians such as Leonhard Euler, Joseph Lagrange, George Green, Simeon-Denis Poisson and others, the mathematical understanding of the elasticity became very strong. Augustus Love summarized all of these theories in his quintessential book,

"*Treatise on the Mathematical Theory of Elasticity*", in 1927. The theory of elasticity suggests that the elastic constants of a material could be determined through measurement of the sound velocities in the material. This gave rise to the idea of conventional time-of-flight measurement with ultrasonic pulses.

Natural frequency measurements were used as early as 1935, but these early methods could only find approximate solutions [6]. Gabriel Lame and Horace Lamb found analytic solutions to the forward problem for a spherical shape with isotropic and noncrystalline materials [19]. These investigations were focused mainly on the Earth after a large earthquake. The geophysics community contributed in this particular problem with a view to determining the Earth's interior structure, and to measure accurately the elastic moduli of materials believed to be earth's constituents [23]. These investigators did not solve the inverse problem for sphere.

In 1964 Fraiser and LeCrew [7] used the solution of the sphere and inverted graphically, which may be the first RUS measurement. Geophysicists Orson Anderson, Naohiro Soga and Edward Schreiber who worked to improve Fraiser and LeCrew's method, introduced the term Resonant Ultrasound Technique (RST). Anderson and Schreiber used RST to measure spherical lunar samples in 1970. In their paper, an observation about the composition of the moon was made and some ancient claims about moon being made of cheese were studied. In Erasmus's collection of Latin proverbs, Adagia's(1452) phrase, "his friends believed the moon to be made of Green cheese" was quoted [2]. Sound speed of different cheeses and lunar rocks were also studied.

Harod Demarest, who was a graduate student of Anderson at Columbia University, first used RST for a cubic shape. He is the first one to approach the forward problem numerically rather than analytically, based on variational principles. The Rayleigh-Ritz technique and integral equations were used by Demarest to define the free vibrations. He referred this technique as *cube resonance*. Mineo Kumazawa, a post-doctoral researcher at Columbia university was pursuing

ultrasonic measurements of minerals during the lunar rocks experiments. He studied Demarest's method and when he returned to Nagoya University, established a laboratory on resonant ultrasound. His graduate student, Ichiro Ohno worked with him to develop the technique. In 1976 Ohno published a paper with some significant development of Demarest's work [26]. In 1988 while working with small piezoelectric film transducers, Migliori and Maynard faced problem with the resonance frequencies and Migliori tracked down the geophysics literature for RUS. Migliori extended the technique and introduced the term *Resonant Ultrasound Spectroscopy*. Even with the limitation of geometry choice, this technique soon proved its usefulness in material science. In the early years the biggest problem was the limitation of computational resources. With the advancement of computing power, RUS is becoming more useful in the field of material research.

Chapter 2

Methodology

2.1 Introduction

Many methods are available to measure the elastic constants of solids. The resonance method was limited to specific shape and crystallographic symmetry. Using the calculus of variations the integral equations for free vibrating elastic bodies are developed. Lets assume an arbitrarily shaped object with elastic tensor C_{ijkl} and density ρ with a free surface S surrounding a volume V. Both quantities(ρ and C_{ijkl}) may vary with the position in V. Let ω be a non-negative real number, $\mathbf{u(r)}$ be a real-valued function of position $\mathbf{r}$ in V. Then the combination of $\{\omega, \mathbf{u}\}$ is a free oscillation or resonance if the real-valued displacement field satisfies

$$\mathbf{s}(\mathbf{r}, t) = \Re(\mathbf{u}(\mathbf{r})e^{i\omega t}) \tag{2.1}$$

the elastic equations of motion in volume V. The analytical solution of this mechanical behavior is next to impossible [34]. In fact for a given volume, for all values of ω there will be no displacement ($\mathbf{u}$) value that will satisfy the boundary condition. To solve the problem a numerical approach is used.

2.2 Formulation of the Problem

We consider conservative systems in which the kinetic and potential energy is function of position only. And the kinetic and potential energy is a function of resonance. Using classical mechanics the Lagrangian of the system is

$$\mathcal{L} = \int_V (E_k - E_p) dV \tag{2.2}$$

Here E_k and E_p are the kinetic and potential energy respectively. The potential energy associated with the displacement $\mathbf{u}$ is given by the strain energy

$$E_p = \frac{1}{2} \int_V C_{ijkl} \frac{\partial u_i}{\partial x_j} \frac{\partial u_k}{\partial x_l} \tag{2.3}$$

Where u_i is the ith ($i = 1, 2, 3$ corresponding to the x, y or z directions in coordinate space) component of the displacement vector $\mathbf{u}$ and we have assumed that the displacements' time dependence is e^{iwt}. The corresponding kinetic energy will be

$$E_k = \omega^2 K \tag{2.4}$$

where

$$K = \frac{1}{2} \int_V \rho u_i u_i dV \tag{2.5}$$

Now the Lagrangian becomes (using Eq. 2.2)

$$\mathcal{L} = \omega^2 K - E_p \tag{2.6}$$

The kinetic and potential energy in the above equation can be calculated for any ω and $\mathbf{u}$. Now it is necessary to find a condition where we can use the above equation for resonance only. In this situation classical mechanics helps by assuming that the quantity $\mathcal{L}$ is *stationary* if and only if ω and $\mathbf{u}$ are a resonance of V. The term *stationary* implies that $\mathcal{L}$ does not change within the volume V and surface S if

the displacement $\mathbf{u}$ is replaced by $\mathbf{u} + \partial\mathbf{u}$.

$$\mathcal{L} \rightarrow \mathcal{L} + \partial\mathcal{L} \tag{2.7}$$

$$\mathcal{L} + \partial\mathcal{L} = \frac{1}{2}\int_V \left[\rho\omega^2(u_i + \partial u_i)^2 - C_{ijkl}\frac{\partial(u_i + \partial u_i)}{\partial x_j}\frac{\partial u_k}{\partial x_l}\right] dV \tag{2.8}$$

Keeping terms to first order in ∂u_i, the change in lagrangian is

$$\partial\mathcal{L} = \int_V \left[\rho\omega^2 u_i \partial u_i - C_{ijkl}\frac{\partial(\partial u_i)}{\partial x_j}\frac{\partial u_k}{\partial x_l}\right] dV \tag{2.9}$$

After integration by parts it yields,

$$\partial\mathcal{L} = \int_V \left(\rho\omega^2 u_i + C_{ijkl}\frac{\partial^2 u_k}{\partial x_j \partial x_l}\right)_i \partial u_i dV + \int_S \left(\vec{\eta}_j C_{ijkl}\frac{\partial u_k}{\partial x_l}\right)_i \partial u_i dS \tag{2.10}$$

Here, $\vec{\eta_j}$ is the normal vector to the surface. The above equation (2.10) can be written in the following form:

$$\partial\mathcal{L} = \int_V (elastic\ wave\ equation)_i \partial u_i dV + \int_S (surface\ traction)_i \partial u_i dS \tag{2.11}$$

Due to the stationary condition the change of Lagrangian has to be zero(i.e, $\partial\mathcal{L} = 0$). To satisfy the condition each of the two terms inside the Equation 2.10 have to be independently zero. Setting the first term of the equation to zero yields the wave equation:

$$\rho\omega^2 u_i + \sum_{j,k,l} C_{ijkl}\frac{\partial^2 u_k}{\partial x_j \partial x_l} = 0 \tag{2.12}$$

The second bracketed term is the expression of the free-surface boundary condition.

$$\sum_{j,k,l} \eta_j C_{ijkl}\frac{\partial u_k}{\partial x_l} = \sum_j \vec{\eta}\sigma_{ij} = 0 \tag{2.13}$$

The above equation represents the ith component of the surface traction vector. Where η_i is the unit vector normal to surface and σ_{ij} is the ij component of

the stress tensor. So the displacement vector u_i which satisfies these conditions (Equation 2.12, 2.13) will represent a singular value of ω; which is one of the normal mode frequencies of free vibration of the system.

2.2.1 Choice of Basis Function

The next step is to turn the displacement vector $\mathbf{u}$ into some mathematical function. One way is to use a simple expansion that can satisfy a range of geometry. Using Rayleigh-Ritz method [29], the displacement vector can be expanded in the following way:

$$u_i = \sum_{\lambda} a_{i\lambda} \Phi_\lambda \tag{2.14}$$

Where $a_{i\lambda}$ are the generalized constants and Φ_λ are a set of *shape functions*. Both of these are linearly independent and satisfying the global kinematic boundary condition. The choice of Φ_λ is arbitrary. Historically, Demarest and Ohno used normalized Legendre polynomials [6] [26]. This had the advantage of dealing with simpler matrices, but it also limits the choice of object shape. Visscher used the following method to expand the *shape function* Φ_λ [32].

$$\Phi_\lambda = x^{l(\lambda)} y^{m(\lambda)} z^{n(\lambda)} \tag{2.15}$$

Where (l, m, n) are discrete element of basis set λ and $l, m, n \in \mathbb{Z}^+$. Equation (2.14) can be written in the following form:

$$u_i = \sum_{(l,m,n)}^{\infty} a_{i(l,m,n)} \Phi_{(l,m,n)} \tag{2.16}$$

The above equation cannot be summed to infinity, thus a truncation condition will be imposed. The truncation condition is:

$$l + m + n \leq N \tag{2.17}$$

The truncation condition will introduce truncation error since Equation 2.16 is not being summed to infinity. In practice N has a number that will compromise between computational time and accuracy. It is a combination problem to find out how many polynomials will appear in the expansion of the displacement. The correct number of combinations is

$$\binom{N+3}{3} = \frac{(N+3)!}{3!(N+3)!} = \frac{(N+1)(N+2)(N+3)}{6} \tag{2.18}$$

2.2.2 Lagrangian in Matrix Form

For a given number of N there are basis elements counting all three components of **u**. Now replacing the displacement vector (Equation 2.14) with the basis function in Equation 2.2 yields the following form.

$$\mathcal{L} = \frac{1}{2}\int_V \left[\rho\omega^2 a_{i\lambda}a_{i'\lambda'}\Phi_\lambda\Phi_{\lambda'}\delta_{ii'} - \frac{1}{2}C_{ijkl}a_{i\lambda}a_{i'\lambda'}\frac{\partial\Phi_\lambda}{\partial x_j}\frac{\partial\Phi'_\lambda}{\partial x_l}\right] dV \tag{2.19}$$

Here $\delta_{ii'}$ is a *Kronecker delta*, which provides following condition

$$\delta_{ii'} = \begin{cases} 1 & \text{if i=i'} \\ 0 & \text{if i}\neq\text{ i'} \end{cases} \tag{2.20}$$

λ and λ' represent two different basis sets. To keep track of all the subscripts in Equation 2.19 the following conditions are required.

i the Cartesian component of **u**
$l(\lambda)$ the component of x in Φ_λ
$m(\lambda)$ the component of y in Φ_λ
$n(\lambda)$ the component of z in Φ_λ

Equation 2.19 can be written in the following matrix equation.

$$\mathcal{L} = \frac{1}{2}\omega^2\mathbf{a}^T E\mathbf{a} - \frac{1}{2}\mathbf{a}^T\Gamma\mathbf{a} \tag{2.21}$$

Where $\mathbf{a}$ is a vector with elements a_i whose transpose is $a^T$and where E and Γ are matrices whose order R (number of columns and rows) is determined by the truncation condition in Equation 2.17. The matrix E has elements

$$E_{\lambda i \lambda' i'} = \delta_{ii'} \int_V \Phi_\lambda \rho \Phi_{\lambda'} dV \tag{2.22}$$

And the matrix Γ has elements

$$\Gamma_{\lambda i \lambda' i'} = C_{ijkl} \int_V \frac{\partial \Phi_\lambda}{\partial x_j} \frac{\partial \Phi_{\lambda'}}{\partial x_{j'}} dV \tag{2.23}$$

If Φ_λ was chosen to be an orthonormal set with respect to the density ρ (Demarest and Ohno did using Legendre polynomials), E would have been a unit matrix and our calculation would be simple. Since our choice of Φ_λ provides a wide range of shapes, it has computational complexity. To simplify the matrices, the following calculation can be followed. Using the K matrix from Equation 2.5:

$$\begin{aligned} K &= \tfrac{1}{2} \textstyle\int_V \rho u_i u_i dV \\ K_{\lambda\lambda'} &= \tfrac{1}{2} \textstyle\int_V \rho \alpha_\lambda x^{l(\lambda)} y^{m(\lambda)} z^{(\lambda)} \delta_{i(\lambda) i'(\lambda)} \times \alpha_{\lambda'} x^{l(\lambda')} y^{m(\lambda')} z^{n(\lambda')} dV \\ &= \tfrac{1}{2} \textstyle\int_V \rho x^{l(\lambda+\lambda')} y^{m(\lambda+\lambda')} z^{n(\lambda+\lambda')} dV \end{aligned} \tag{2.24}$$

There is a similar but complicated expansion of matrix E. In both cases the result has similar integral form as follows.

$$\int_V f(x,y,z) x^l y^m z^n dV \tag{2.25}$$

Where $f(x,y,z)$ is either density for matrix E or one of the Cartesian components of the elastic stiffness tensor. In any region (constant S and volume V) in which $f(x,y,z)$ can be written as a monomial basis function, a condition that includes the nearly universal case of being constant in S, all of the integrals are in the

following form:

$$\mathcal{I}(l,m,n) = \int_S x^l y^m z^n dV \tag{2.26}$$

All of these problems reduce to the evaluation of the integral from the above equation, which is sometimes referred as *geometric* integral. Matrix E and Γ can be re-written in the following way.

$$E_{\lambda i \lambda' i'} = \int_V \rho x^l y^m z^n dV = \rho \mathcal{I} \tag{2.27}$$

$$\Gamma_{\lambda i \lambda' i'} = \int_V C_{ijkl} f(x,y,z) x^l y^m z^n dV = C_{ijkl} f(x,y,z) \mathcal{I} \tag{2.28}$$

2.2.3 Generalized Eigenvalue Equation

Equation 2.2 for Lagrangian is stationary if the displacements u_i are solutions of the free-vibration problem. These solutions may be obtained by setting the derivatives of Equation 2.21 to zero with respect to each of the R amplitude $a_{i\lambda}$. Since $\delta\mathcal{L} = 0, \quad \partial\mathcal{L}/\partial a_{i\lambda} = 0$, this yields the following equation:

$$\omega^2 E\mathbf{a} = \Gamma\mathbf{a} \tag{2.29}$$

Equation 2.29 is the *generalized symmetric eigenvalue problem* and is readily solved with modern software. This is the ultimate equation that is solved to get the resonance frequencies. Here eigenvalues are ω^2 and the eigenvectors are $\mathbf{a}$. Thus, calculating the resonant frequencies for a 3D elastic body is essentially one of calculating the matrices Γ and E. The special vectors $\mathbf{a}$ are the *mode shapes* of the system. These are the special initial displacements that will cause the mass to vibrate harmonically.

Now the problem is reduced to correctly determining the matrices E and Γ. To explain how to generate these matrices a simple geometry with high symmetry will be used. The most frequently used sample geometry for RUS is the rectangular parallelepiped (RP). Here we are assuming that the crystallographic axes align

with the sample faces and with orthorhombic or higher crystal symmetry. The mathematical development is summarized in the following flow chart Figure 2.1.

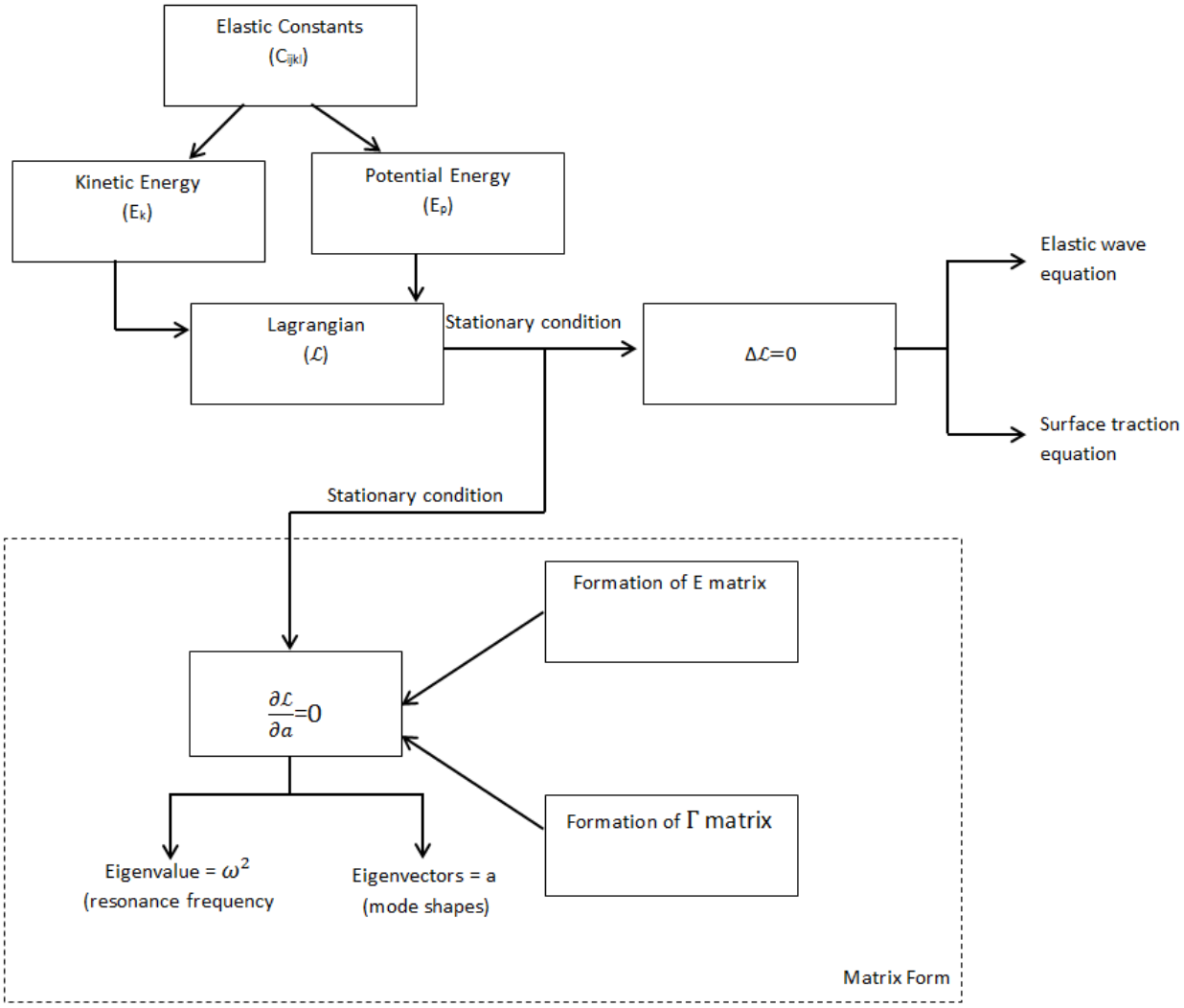

Figure 2.1: Flow chart of the mathematical development of a typical RUS problem

2.2.4 Example:Calculation of Resonance frequencies of Rectangular parallelepiped

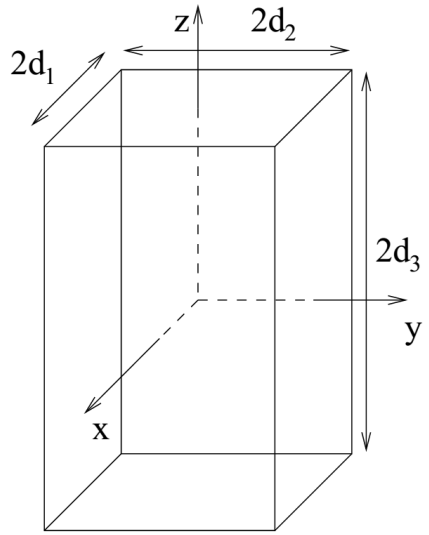

Figure 2.2: Dimension associated with rectangular parallelepiped(RP)

For a RP of sides $2d_1$, $2d_2$, $2d_3$ (Figure 2.2), the integral in Equation 2.26 can be evaluated explicitly to give

$$\mathcal{I}(l,m,n) = \frac{8d_1^{l+1}d_2^{m+1}d_3^{n+1}}{(l+1)(m+1)(n+1)} \tag{2.30}$$

To get the above integral form some assumptions were made. In order to simplify matrix Γ, we have to understand the elastic constant C_{ijkl} and how it can be minimized using isotropic assumptions. To generate matrix E and Γ for rectangular parallelepiped, a Matlab code is given in appendix A. This code is written based on Visscher's XYZ algorithm [32]. And the generalized eigen function equation solved using Matlab's *eig* function.

2.3 Basics of Elasticity

When a force, either internal or external, is applied to a continuum every point of this continuum is influenced by this force. Internal force is referred as *body force*

and external force as *contact force*. Gravity is an example of body force. Body forces are proportional to the volume of the medium and to its density. Contact forces depend on the surface they are acting on.

If an external force acts on a continuum, it will lead to deformation (changes of size and shape) of the medium. Internal forces acting within the medium will try to resist this deformation. As a consequence the medium will return to its original shape and volume when the external forces are removed. If this recovery of this original shape is perfect, the medium is called is *elastic*. The law relating the applied force to the deformation is called *Hooke's Law*. It is defined by stress and strain. Hooke's law states that the strain is linearly proportional to stress or conversely, that the stress is linearly proportional to stress [3]. The second form is stated by writing each component of stress (elastic restoring force) as a general linear function of all the strain components. The generalized form will be

$$\begin{aligned}\sigma_{xx} = C_{xxxx}\epsilon_{xx} + C_{xxxy}\epsilon_{xy} + C_{xxxz}\epsilon_{xz} + \\ C_{xxyx}\epsilon_{yx} + C_{xxyy}\epsilon_{yy} + C_{xxyz}\epsilon_{yz} + \\ C_{xxzx}\epsilon_{zx} + C_{xxzy}\epsilon_{zy} + C_{xxzz}\epsilon_{zz} \quad (2.31)\end{aligned}$$

The above equation can be written in the following form

$$\sigma_{ij} = C_{ijkl}\epsilon_{kl} \quad with\ i, j, k, l = x, y, z \quad (2.32)$$

Here C_{ijkl} are the components of the fourth-order *stiffness* tensor of material properties or *Elastic moduli*. The fourth-order stiffness tensor has 81 constants and 16 components for three-dimensional problem. The stress tensor σ_{ij} completely describes the state of stress at any point p of the continuum.

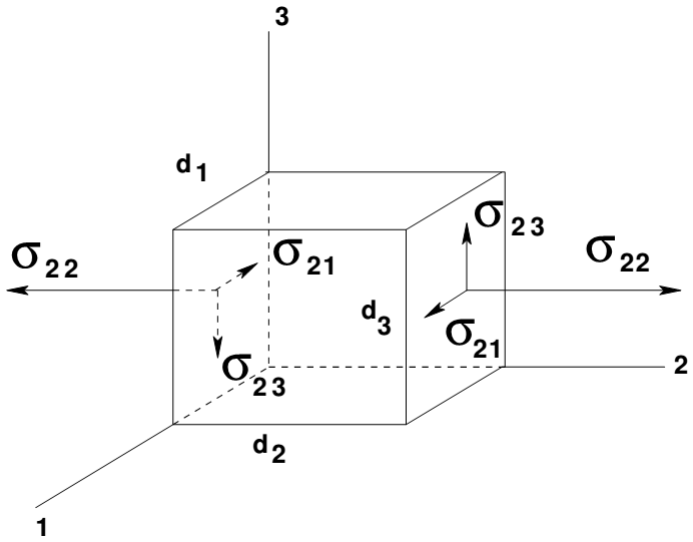

Figure 2.3: Stress component on a particular point

$$\sigma_{ij} = \begin{pmatrix} \sigma_{11} & \sigma_{12} & \sigma_{13} \\ \sigma_{21} & \sigma_{22} & \sigma_{23} \\ \sigma_{31} & \sigma_{32} & \sigma_{33} \end{pmatrix} \quad with\ i,j = 1,2,3 \tag{2.33}$$

Equation 2.32 contains nine equations (corresponding to all possible combinations of the subscripts ij) and each equation contains nine strain variables. Due to the symmetry of strain and stress tensors the stiffness tensor reduces to a smaller number. Using the symmetry of stress tensor:

$$\sigma_{ij} = \sigma_{ji} \Longrightarrow C_{ijkl} = C_{jikl} \tag{2.34}$$

This reduces the number of stiffness constants from $81 = 3 \times 3 \times 3 \times 3 \rightarrow 54 = 6 \times 3 \times 3$. Similarly using the symmetry of strain tensor:

$$\epsilon_{ij} = \epsilon_{ji} \Longrightarrow C_{ijkl} = C_{jikl} \tag{2.35}$$

This reduces the material constants to $36 = 6 \times 6$. To reduce the size of the material constants we can use the symmetry property of the tensor itself. Which

is

$$C_{ijkl} = C_{klij} \tag{2.36}$$

This further reduces the number of material constants to 21. The most general anisotropic (triclinic crystal structure) linear elastic material therefore has 21 elastic constants. Now the stress-strain relationship can be written as follows

$$\begin{bmatrix} \sigma_{11} \\ \sigma_{22} \\ \sigma_{33} \\ \sigma_{23} \\ \sigma_{13} \\ \sigma_{12} \end{bmatrix} = \begin{bmatrix} C_{1111} & C_{1122} & C_{1133} & C_{1123} & C_{1113} & C_{1112} \\ & C_{2222} & C_{2233} & C_{2223} & C_{2213} & C_{2212} \\ & & C_{3333} & C_{3323} & C_{3313} & C_{3312} \\ & symm & & C_{2323} & C_{2313} & C_{2312} \\ & & & & C_{1313} & C_{1312} \\ & & & & & C_{1212} \end{bmatrix} \begin{bmatrix} \epsilon_{11} \\ \epsilon_{22} \\ \epsilon_{33} \\ 2\epsilon_{23} \\ 2\epsilon_{13} \\ 2\epsilon_{12} \end{bmatrix} \tag{2.37}$$

Since the $3 \times 3 \times 3 \times 3$ tensors become 6×6, we can use general matrix notation to explain the stress-strain relation. With these constraints on the stiffness constants the four subscript on the tensor may be reduced to two by using abbreviated subscript notation, where

I	ij
1	xx
2	yy
3	zz
4	yz, zy
5	xz, zx
6	xy, yx

$$[C] = \begin{bmatrix} C_{11} & C_{12} & C_{13} & C_{14} & C_{15} & C_{16} \\ & C_{22} & C_{23} & C_{24} & C_{25} & C_{26} \\ & & C_{33} & C_{34} & C_{35} & C_{36} \\ & symm & & C_{44} & C_{45} & C_{46} \\ & & & & C_{55} & C_{56} \\ & & & & & C_{66} \end{bmatrix} \tag{2.38}$$

The above equation shows the elastic constants for a complete anisotropic material, which has 21 elastic constants. When the material has symmetry within its structure the number of elastic constants reduces even further.

2.3.1 Elastic Isotropy Conditions

It is necessary to determine the restrictions imposed by elastic isotropy on stiffness matrices. In an isotropic medium the three coordinates axes, x,y,z and the three coordinate planes yz, xz, xy are equivalent. This means the elastic constants are independent of the direction of the axes. Consequently, the response of the medium must be the same for a compressive stress applied along any axis. Therefore:

$$\epsilon_{11} = \epsilon_{22} = \epsilon_{33}$$
$$\epsilon_{12} = \epsilon_{13} = \epsilon_{23}$$

Also, the shear strain produced in a coordinate plane by a shear stress applied in that plane must be the same for all coordinate planes,

$$\epsilon_{44} = \epsilon_{55} = \epsilon_{66}$$

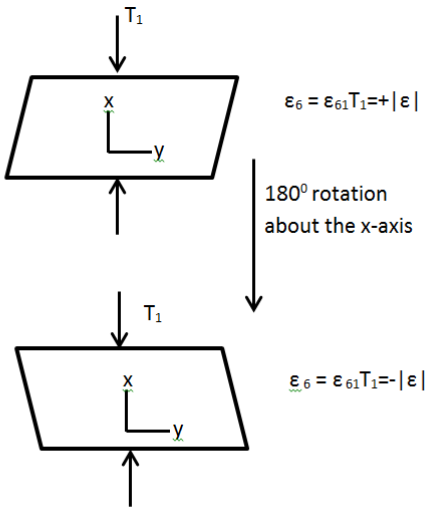

Figure 2.4: Symmetry logic proves that $\epsilon_{61} = -\epsilon_{61} = 0$ in an isotropic medium

Now, dealing with other shear strains, suppose that a compressive stress T_1

applied along the x axis produces a shear strain ϵ_6 in the xy plane. Due to the isotropic property if the plane is rotated 180^0 about the x axis, an equal valid solution to the applied stress T_1 will exist. This reverses the sign of the ϵ_6, which can therefore only be zero. Hence

$$\epsilon_{16} = 0$$

Similarly

$$\epsilon_{14} = \epsilon_{15} = \epsilon_{24} = \epsilon_{25} = \epsilon_{26} = \epsilon_{34} = \epsilon_{35} = \epsilon_{36} = 0$$

Similarly using the same argument in a different coordinate plane it can be shown that

$$\epsilon_{45} = \epsilon_{46} = \epsilon_{56} = 0$$

The above conditions can be applied to the elastic stiffness matrix (equation 2.38). When these conditions are used the matrix becomes

$$[C] = \begin{bmatrix} C_{11} & C_{12} & C_{12} & 0 & 0 & 0 \\ & C_{11} & C_{12} & 0 & 0 & 0 \\ & & C_{11} & 0 & 0 & 0 \\ & symm & & C_{44} & 0 & 0 \\ & & & & C_{44} & 0 \\ & & & & & C_{44} \end{bmatrix} \tag{2.39}$$

The above expression for the elastic constants may be sufficient for the isotropic material. And it is also similar to the stiffness matrix of the cubic material. But using the rotation over the z axis it can be shown that[3] the condition for invariance of matrix [C] for an isotropic material is

$$C_{12} = C_{11} - 2C_{44} \tag{2.40}$$

This same condition can be obtained using rotation about the y axis or x axis.

From equation 2.44 and 2.40 it is clear that for an isotropic medium there are only two independent elastic constants. These are often called *Lamé constants* λ and μ, defined by

$$\begin{aligned} \lambda &= C_{12} \\ \mu &= C_{44} \end{aligned}$$

Using the Lamé constants the stiffness matrix can be represented in the following way:

$$[C] = \begin{bmatrix} \lambda+2\mu & \lambda & \lambda & 0 & 0 & 0 \\ & \lambda+2\mu & \mu & 0 & 0 & 0 \\ & & \lambda+2\mu & 0 & 0 & 0 \\ & symm & & \mu & 0 & 0 \\ & & & & \mu & 0 \\ & & & & & \mu \end{bmatrix} \tag{2.41}$$

Lamé constant μ is referred to as *shear modulus*, which is the measure of the shear stress. The second Lamé constant λ is important as a combination with other elastic constants, e.g., the Young's modulus E, the bulk modulus K, and Poisson's ratio ν.

2.3.2 Engineering Constants

Equation 2.32 provides the linear relationship between stress (σ_{ij}) and strain (ϵ_{kl}). Alternatively, the strains may be expressed as a general linear function of the stresses,

$$\epsilon_{ij} = \mathcal{S}_{ijkl}\sigma_{kl} \tag{2.42}$$

Here $\mathcal{S}_{ijkl}$ is called *compliance constants*, which is the inverse of the stiffness matrix (Equation 2.38). That is:

$$[\mathcal{S}] = [C]^{-1} \tag{2.43}$$

The compliance constants for an isotropic medium can be obtained by taking inverse of the stiffness matrix of the isotropic medium (2.44). Matrix C has dimensions of 6×6, so the inverted matrix will also have the same dimensions. So the compliance matrix will be

$$[\mathcal{S}] = \begin{bmatrix} \mathcal{S}_{11} & \mathcal{S}_{12} & \mathcal{S}_{12} & 0 & 0 & 0 \\ & \mathcal{S}_{11} & \mathcal{S}_{12} & 0 & 0 & 0 \\ & & \mathcal{S}_{11} & 0 & 0 & 0 \\ & symm & & \mathcal{S}_{44} & 0 & 0 \\ & & & & \mathcal{S}_{44} & 0 \\ & & & & & \mathcal{S}_{44} \end{bmatrix} \tag{2.44}$$

with

$$\mathcal{S}_{11} = \frac{C_{11} + C_{12}}{(C_{11} - C_{12})(C_{11} + 2C_{12})}$$

$$\mathcal{S}_{12} = \frac{-C_{12}}{(C_{11} - C_{12})(C_{11} + 2C_{12})}$$

$$\mathcal{S}_{44} = \frac{1}{C_{44}}$$

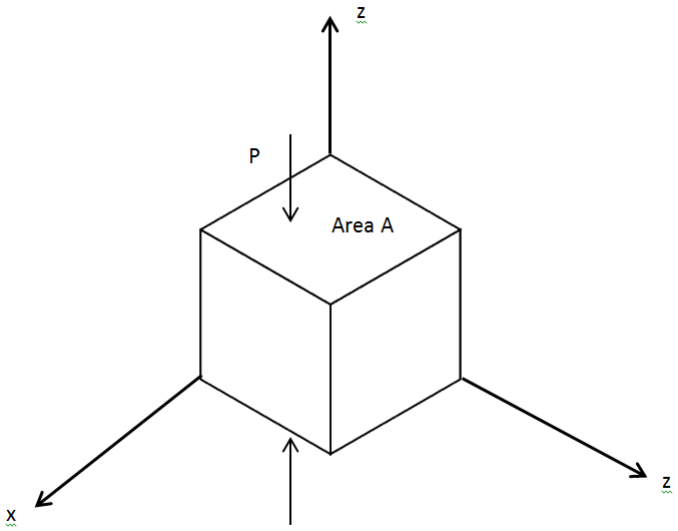

Figure 2.5: Isotropic object subjects to pressure P

Now, an isotropic parallelepiped (Figure 2.5) is subject to static pressure P on

one end and is unconstrained on its sides. Then the strain field will be:

$$\epsilon_{11} = \mathcal{S}_{12}\frac{p}{A}$$

$$\epsilon_{22} = \mathcal{S}_{12}\frac{p}{A}$$

$$\epsilon_{33} = \mathcal{S}_{11}\frac{p}{A}$$

Poisson's ratio, ν, provides information about the ratio between lateral and longitudinal strain in uniaxial tensile stress. Using the condition in Figure 2.5, ν can be written in the following form using strains:

$$\nu = -\frac{\epsilon_{11}}{\epsilon_{33}} = -\frac{\epsilon_{22}}{\epsilon_{33}} = \frac{\mathcal{S}_{12}}{\mathcal{S}_{11}} = \frac{C_{12}}{C_{11}+C_{12}} = \frac{\lambda}{2(\lambda+\mu)} \tag{2.45}$$

And Young's modulus is defined by

$$Y = \frac{\sigma_{33}}{\epsilon_{33}} = \frac{1}{\mathcal{S}_{11}} = \frac{(C_{11}-C_{12})(C_{11}+2C_{12})}{C_{11}+C_{12}} = 2\mu(1+\nu) \tag{2.46}$$

2.4 Hollow Tube Geometry

The shape of the object for RUS experiment has an important impact on the forward calculation, as it influences the mode selection. Mode shape identification and frequency analysis for different compact geometries have been done for cylinders [11], spheres [15], cubes [6] and rectangular parallelepiped [32]. It is also done for arbitrary shapes which is called 'potato' [32]. The regular shapes were studied as these are the obvious choice for fundamental mechanical property studies. However, hollow cross sections were also studied in the context of carbon nano tubes, both analytically [21] and numerically [16]. Jaglinski and Wang [14] did a study to calculate the resonance frequencies for the hollow geometry using RUS. But they kept their experiment limited to very small object. Even though the Rayleigh-Ritz method creates mathematical complexity for the arbitrarily shaped geometry, finite element method (FEM) provides a very good solution. The fun-

damental assumptions of RUS is the stress free surface of the object. But a hollow geometry creates another surface inside the object. This condition makes the integration part difficult to calculate with proper boundary condition. On the other hand defining a geometry with FEM can be less arduous. Since FEM converts the system of partial differential equations to linear algebraic system, proper boundary conditions can be provided in the interested region. So for this thesis FEM was used for the calculation of the resonance frequencies. Commercial finite element package, Abaqus, is used for this purpose.

2.5 Classical Solution of Vibrating rings and tubes

The equations of motion for an isotropic elastic medium are,

$$(\lambda + \mu)\frac{\partial^2 u_j}{\partial x_j \partial x_i} + \mu \frac{\partial^2 u_i}{\partial x_j \partial x_j} = \rho \frac{\partial^2 u_i}{\partial t^2} \tag{2.47}$$

Here λ and μ are Lamé constants, subscripts i and j are labels for spatial dimensions, ranging from 1 to 3, t denotes time, and ρ is mass density. To derive the resonant frequencies for the free vibration problem, the required boundary conditions are $\sigma_{zz} = \sigma_{zr} = \sigma_{z\theta}$ on the $z = 0$ and $z = L$ surfaces, $\sigma_{rr} = \sigma_{r\theta} = 0$ on the $r = a$ and $r = b$ cylindrical surfaces. There is no analytical solution for the general problem. Analytical solutions to some of the mechanical systems are presented in the following discussions.

For thin, narrow, annular rings the resonant frequencies were obtained by Hoppe in 1872 [12]. It was done for flexural vibrations, in which flexural vibrations travel around the ring. Later, in 1889, Rayleigh [30] found the solution of the finite frequency spectrum regarding extensional (rod) waves. For a thin disk the in-plane vibrations are radial and torsional waves, and each of the problems can be solved separately. When these vibrations occur together the simultaneous solution of both wave equations is necessary. For short isotropic cylinders with length equal to diameter the elastic constant can be found in the following way. As torsion being the fundamental resonant mode [33].

$$f_{torsion} = k_{sh}\sqrt{\mu/\rho} \tag{2.48}$$

Where frequency in hertz ($f = \omega/2\pi$), $f_{torsion}$ is the resonant frequency, k_{sh} is the shape factor with units of 1/m, μ is the isotropic shear modulus in pa, and ρ is the material density in kg/m^3. For cubes [6] $k_{sh} = \sqrt{2}/(\pi L)$ and for cylinders of length equal to diameter [11], $k_{sh} = 1/(2L)$. In both cases, L is the sample

length. Flexural vibrations include both displacement at right angles to the plane and twist. Flexural vibrations can be determined using following equation [19].

$$f_{flex}^2 = \frac{Ec^4}{16\pi ma^4}\frac{n^2(n^2-1)^2}{(n^2+1)} \tag{2.49}$$

Where the radius of the cross-section is c and the central-line radius of the ring is a. Torsional vibrations, similar to torsional vibrations of a straight rod, correspond to twist of the cross-section about its centerline. For a complete circular ring there are vibrations of this type with n wave-lengths to the circumference, and the frequency f_{tor} is given by the equation [19].

$$f_{tor}^2 = \frac{\mu c^2}{16\pi ma^2}(1+\nu+n^2) \tag{2.50}$$

Extensional vibrations are again similar to the extension of a straight rod and are given by the following equation.

$$f_{ext}^2 = \frac{Ec^2}{4\pi ma^2}(1+n^2) \tag{2.51}$$

When n=0, the tube vibrates radially so that the central-line forms a circle of periodically variable radius appearing as ring breathing, and the cross sections move without rotation. The propagation of the free harmonic waves in an infinitely long cylindrical rod has been discussed by Pochhammer [28] on the basis of the linear theory of elasticity. Gazis determined the frequency equations for several modes for long thick walled tubes under plane strain assumptions which is similar to ring bending [8]. The analytical solutions are only presented for the shell approximation, or $h/a \ll 1$ where h is the tube wall thickness and a is the center-line radius of the ring. Extensional mode (different from previous extensional vibration) frequencies can be approximated by the following equation.

$$f_{ext'} = \frac{n}{2h}\sqrt{\frac{\lambda+2\mu}{\rho}}\left[1+\frac{7-15\nu}{8(1-\nu)(n\pi)^2}\left(\frac{h}{a-h/2}\right)^2\right] \tag{2.52}$$

The resonant frequency for ring extensional vibration is given by the following equation.

$$f_{ring-ext} = \frac{1}{\pi(2a-h)}\sqrt{\frac{\mu}{\rho}}\sqrt{\frac{n^2+1}{2(1-\nu)}} \tag{2.53}$$

Chapter 3

Results

3.1 Identification of Natural Frequencies

The experimental findings of the resonance frequencies and the quality factor (Q)

Table 3.1: Experimentally determined frequencies and quality factor

frequency (MHz)	quality factor (Q)
0.249761819	877312.77
0.2526230818	3167.592128
0.2857712602	190108
0.3019532575	55356.90235
0.31732144539	1498.89148
0.3460458839	293331
0.665954311	2685.039
0.7051525159	3425.08
0.7051581863	3713.762477
0.7051629068	4064.33731
0.7051843006	5951.792446
0.7304325851	327404.79
0.7305864031	10031233
0.74005	241.846406
0.7677167502	4341.86
0.7677167546	4341.3096
0.7731016531	4776.810647
0.8186399228	2726.07707
0.8186410207	3299.974205
0.8200538496	4022.98197
0.8569976883	3169.833879
1.002378015	22994476.462
1.102426855	377.3408
1.201872122	4495.623
1.255168378	905.498

for a hollow cylinder (length = 0.161 m, inner diameter = 0.025 m, outer diameter=0.029 m) are in Table 3.1.

The quality or Q factor associated with a frequency is defined as

$$Q = \frac{f}{\Delta f} \tag{3.1}$$

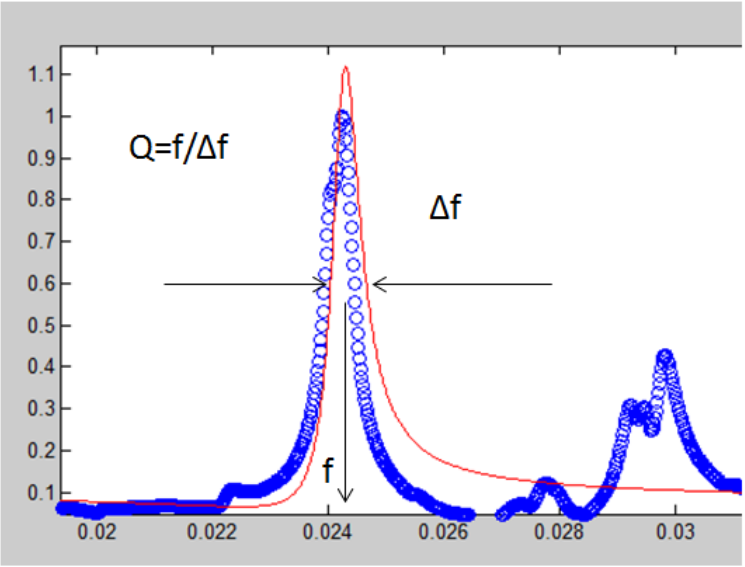

Figure 3.1: An example of measuring Q factor using Lorentzian distribution

Where Δf is the full width at half maximum (FWHM), or the frequency width at the 3 dB points on the power spectrum around frequency. Q is inversely related to attenuation, so low Q materials have high losses [25]. Finding the resonance frequency based on the Q value is very arduous for a wide range of frequency. The curve fitting was done using a matlab code from Zadler and Le Rousseau [35] which is availabe at reference [5]. After getting all the Q values, sorting the frequencies based on the Q values is also critical. This Q value is sometime called intrinsic Q, since the object is loosely coupled with apparatus.

Splitting of the resonance frequencies is shown in Figure 3.2, which shows spectra for a good peak and two defective peaks. When the peaks overlap strongly, it may be impossible to detect splittings without the phase information. To solve that problem selective excitation is used in the particular frequency ranges. For-

tunately some of the modern machines (Lock-in amplifier) can also detect phase information along side the amplitude response. Phase information can help to separate closely attached peaks.

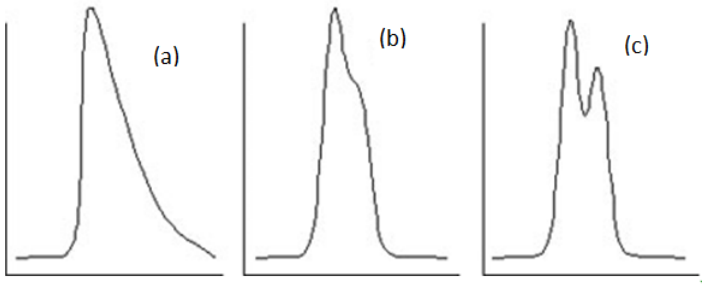

Figure 3.2: Resonance spectrum of a perfect bearing element(a), one with small flaw (b), and one with large splitting (c)

There are many reasons for splitting of peaks. It is usually happens for the non-symmetry or anisotropy in the sample. Phase information gives some flexibility in identifying the overlapping peaks. The sensitivity of the phase information provides good information when the Q value is low or an additional mode is present [25].

3.2 Calculation of the Elastic Constant

Calculation of elastic constants from resonant frequencies is usually called the inverse process. This is an essential part of RUS. For isotropic crystal structure the relation between the Young's modulus (E) and shear modulus (μ) can be found in Equation 2.45 and 2.46. The values for C_{11} and C_{44} can then be obtained through the relation

$$C_{11} = \frac{E(1-\nu)}{(1+\nu)(1-2\nu)} \tag{3.2}$$

and

$$C_{44} = \mu \tag{3.3}$$

For the iteration process the value of C_{11} was varied until the smallest error was found. For this process the Poisson's ratio is kept constant at 0.33 and the other values are changed (Figure 3.3). Young's and shear modulus is related by the following equation

$$E = 2\mu(1+\nu) \tag{3.4}$$

The two elastic moduli C_{11} and C_{44} are related by

$$C_{44} = \frac{C_{11}(1-2\nu)}{2(1-\nu)} \tag{3.5}$$

Since C_{44} is dependent on C_{11}, only C_{11} was varied from a guessed value.

For the Rayleigh-ritz method, the inverse problem (resonance frequency $\rightarrow$ elastic moduli) uses Levenberg-Marquardt algorithm [25], which is known as the damped least-squares method for non-linear system. But for FEM the inverse problem becomes complicated. A good solution has been developed by Plesek et al [27] for FEM. Another modified application of FEM of the inverse problem would be to use initial guesses for the elastic constants and FEM to calculate the resonance frequencies. This process is highly time consuming. The result depends on a good initial guess of the elastic constants. The process of inverting the resonance

frequencies to elastic constants is shown in Figure 3.3.

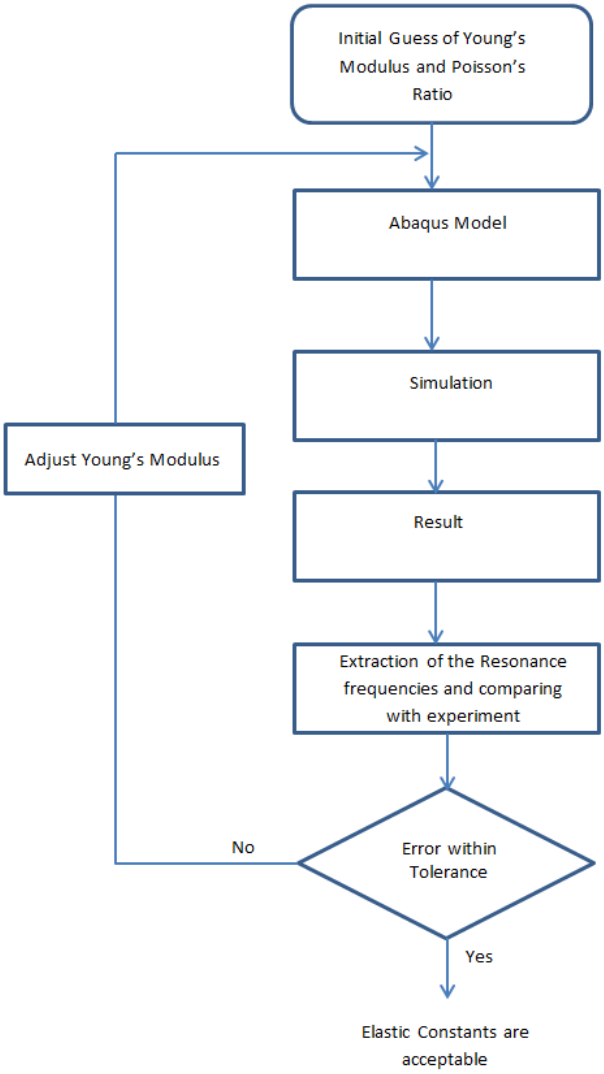

Figure 3.3: Algorithm used to invert the resonance frequencies to elastic constants

Since C_{11} and C_{44} are the two elastic moduli being calculated and are related by equation 3.4 only one of the elastic constants was guessed by guessing the Young's modulus. After several guesses of the Young's modulus the satisfactory values of the error and the calculated frequencies were obtained and are shown in the following table. In Table 3.2 the calculation is shown for $C_{11} = 102.826 \times 10^9$ Pa and $C_{44} = 26.1 \times 10^9$ Pa which corresponds to Young's modulus of 69.39 GPa and Poisson's ratio of 0.33.

Table 3.2: Measured and Computed natural frequencies in MHz for the aluminum cylinder

f_{expt}	f_{calc}	$\lvert\%err\rvert = \lvert\frac{f_{expt}-f_{calc}}{f_{expt}}\rvert$
0.249761819	0.249137414	0.25
0.2526230818	0.251966262	0.26
0.2857712602	0.283227842	0.89
0.3019532575	0.298148646	1.26
0.31732144539	0.327634392	3.25
0.3460458839	0.349125692	0.89
0.665954311	0.661625608	0.65
0.7051525159	0.699088204	0.86
0.7051581863	0.706004376	0.12
0.7051629068	0.702906385	0.32
0.7051843006	0.701869934	0.47
0.7304325851	0.725684773	0.65
0.7305864031	0.728248527	0.32
0.7400500000	0.74108607	0.14
0.7677167502	0.761037614	0.87
0.7677167546	0.769712821	0.26
0.7731016531	0.763824433	1.2
0.8186399228	0.817739419	0.11
0.8186410207	0.805542764	1.6
0.8200538496	0.823334065	0.4

3.3 Mode Identification

The mode identification process was carried out for a complete FEM model of a hollow cylinder. The first model was a small cylinder with L/D (outer diameter) ratio of 1.56 with the same inner and outer diameter of the cylinder that we are interested. The resulting modes and frequencies are compared with Jaglinski and Wang [14] and Li et. al.[16]. The identified modes are described in the following paragraph. After identiying the fundamental modes, the length of the cylinder was increased ($L/D = 6.4$).

The deformed shape obtained from the FEM analysis can be classified into the following categories. S modes are longitudinal shearing, LB modes are longitudinal bending, B modes are barreling or breathing modes. F modes are circumferential, sometimes called flexural, which can be viewed as sinusoidal curve around the surface [16]. Symmetric and antisymmetric F modes exist, in symmetry cases the sinusoids at the end of the tube are in phase and for anti-symmetry they are out of phase. Flexural Bending (FB) modes are both symmetric and antisymmetric ring bending, combined with a barreling deformation. Some of these modes are highly dependent upon the length of the tube. To understand the length effect on the mode identification, four different simulations were done base on four different L/D ratios. The experiment was done for L/D ratio of almost 6.4, which is a fairly long length (0.161 m). Some of the modes are hard to identify for a long length. For a small L/D ratio it is hard to identify any mode below torsional. If the L/D ratio increases, after a certain limit some of the modes create a "wave on string" effect.

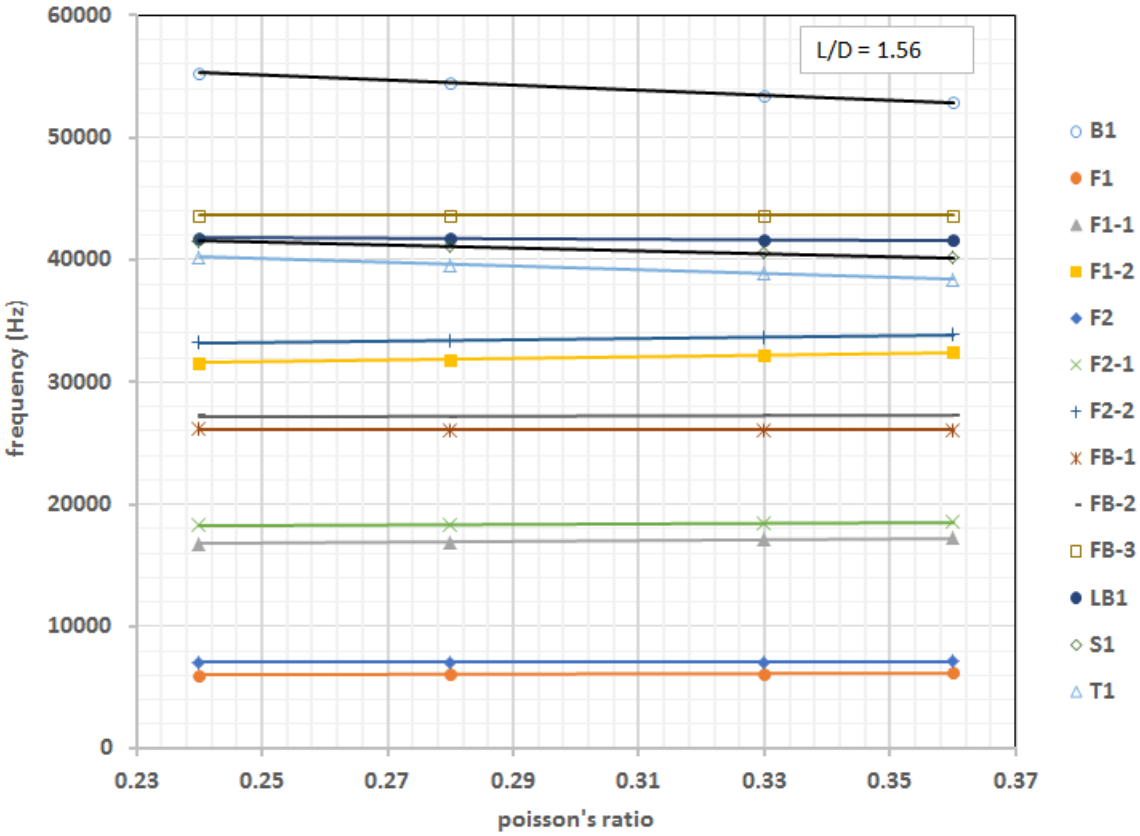

Figure 3.4: Behavior of the modes with the change of the Poisson's ratio

Figure 3.4 shows the change of the location of the modes with the change of the Poission's ratio for small ring (L/D = 1.56). Fundamental torsional mode (T1) and shear mode (s1) do not change with the change of the Poison's ratio. Barreling mode or breathing mode shows a decreasing trend. First and second flexural bending mode (FB-1 and FB-2) do not change with the change of Poisson's ratio too.

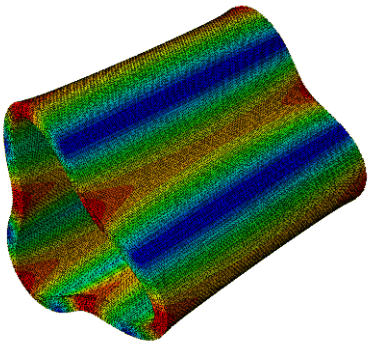

(a) F1-1

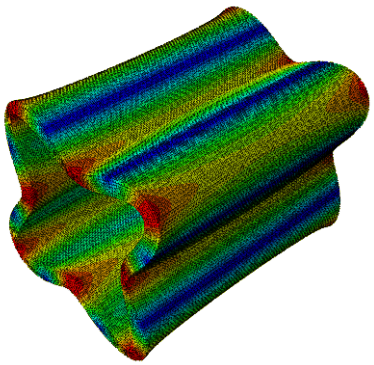

(b) F1-2

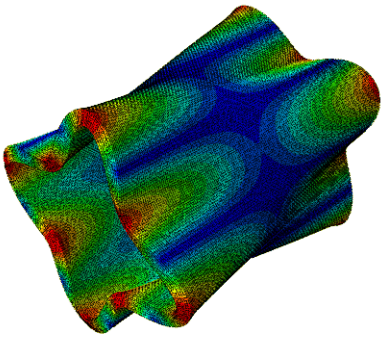

(c) F2-1

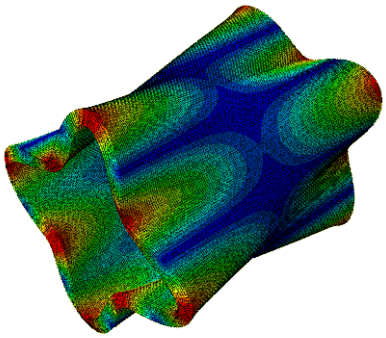

(d) F2-2

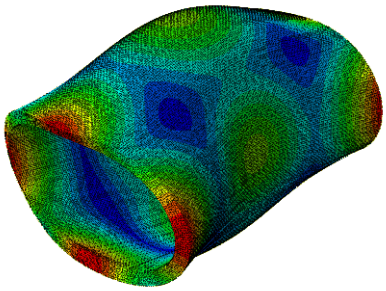

(e) FB-1

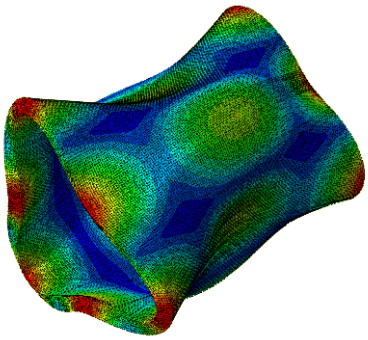

(f) FB-2

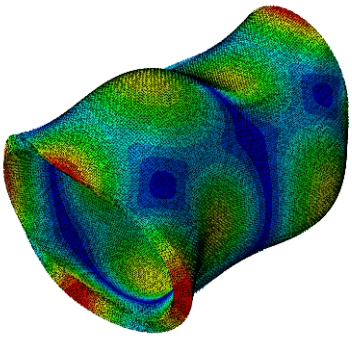

(g) FB-3

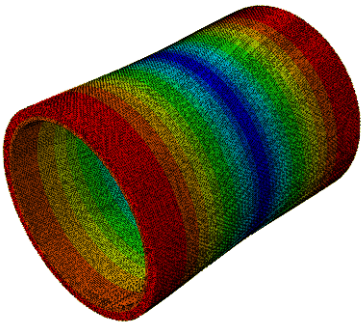

(h) T1

Figure 3.5: Mode shapes and their harmonics for the lowest modes for L/D=1.56(ν = 0.33). The shading intensity is proportional to the element displacements.

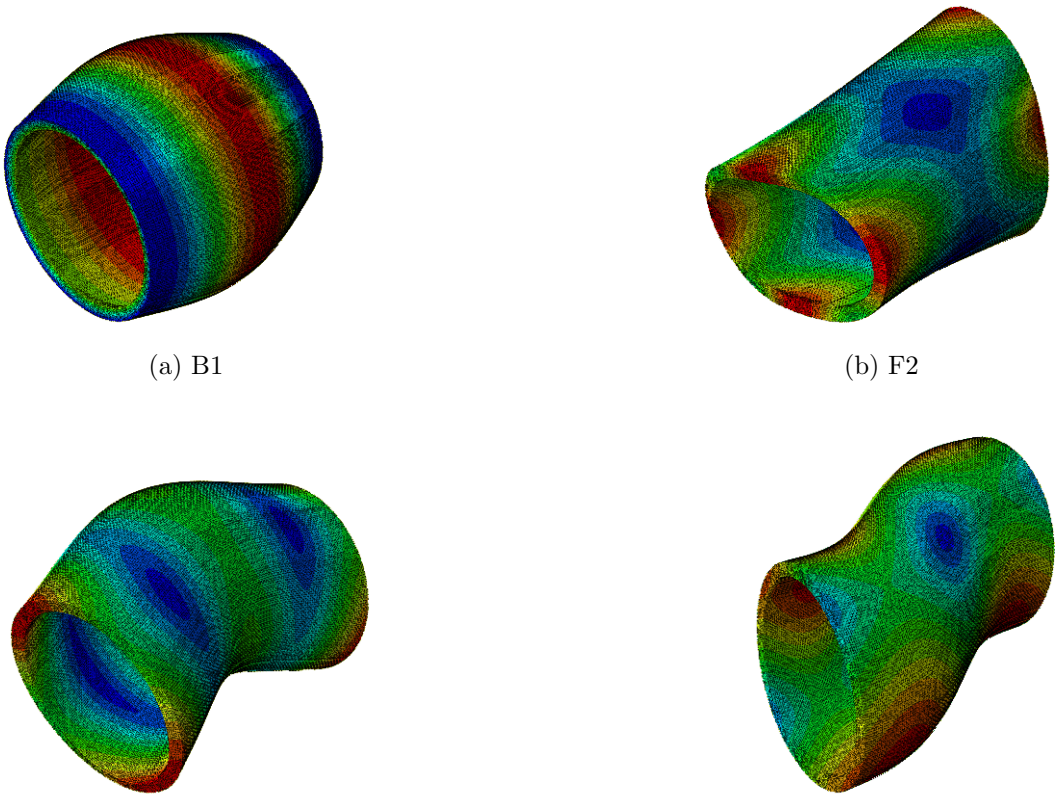

(a) B1 (b) F2

(c) LB1 (d) S1

Figure 3.6: Mode shapes and their harmonics for the lowest modes for L/D = 1.65($\nu = 0.33$).

It is known that lowest vibrational modes of finite length and high aspect ratios are dominated by bending and ring bending, or, "wave-on-a-string, [16]" modes, similar to infinitely long tubes [9][8]. Some of the lowest modes are hard to distinguish for long tube. Flexural behaviour of the infinitly long tube influences the lowest modes. The ratio of the inner to outer diameter ($\Lambda = ID/OD$) also influences the mode shapes and the frequency location.

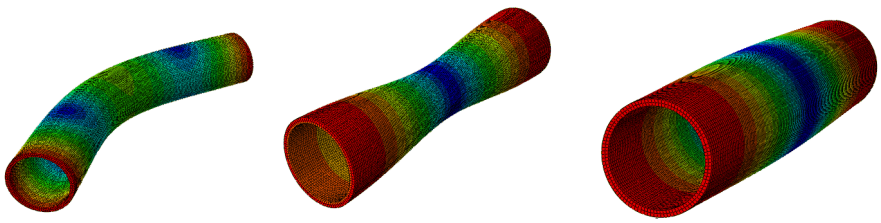

(a) LB1 (b) SA-1 (c) T1

Figure 3.7: Mode shapes for the lowest mode for L/D=6.4($\nu = 0.33$).

Jaglinski and Wang [14] studied the effect of $\Lambda = ID/OD$ in the mode shape and frequency. For the present study the value of Λ is 0.881. According to Jaglinski and Wang when $0 < \Lambda < 0.3$ the fundamental mode is T1. For $\Lambda > 0.3$ the fundamental mode becomes the antisymmetric ring bending mode F1 [14]. The first torsional mode is independent of Λ. For higher values of Λ some of the modes overlap and the harmonics of F and FB modes shift to above 250 kHz. The change of modes with respect to Poisson's ratio is shown in Figure 3.8. The three modes for the long tube(target size, $\Lambda = 0.881$) were studied in this case. To understand a wide range change of mode change, Figure 3.4 provides a very good example.

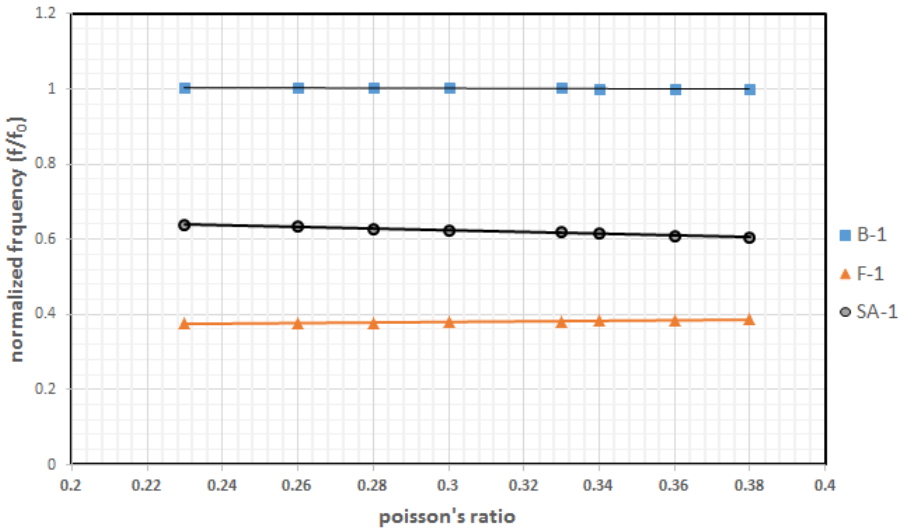

Figure 3.8: Behavior of mode depend on ν(Poisson's ratio) normalized to the first torsional mode(LB1, first longitudinal bending mode; SA 1, Symmetric axial mode; F1, flexural mode).

Change of Young's modulus has a profound impact on the mode frequency. To see how the mode changes with respect to Young's modulus, five different simulations were completed with different Young's moduli. The result of the simulation is shown in Figure **??**. For these simulations, the actual target size cylinder was used. For the initial three modes the change shows a similar pattern. To understand the impact of changing only the Young's modulus, the shape and Poisson's ratio were unchanged.

Chapter 4

Discussions and conclusions

The goals of this thesis were to explore the potential of RUS methods for long cylindrical tubes, study the contact pressure between the two cylinders in target, and the usefulness of this technique in assessing target damage due to radiation. The results obtained from RUS are highly dependent on the choice of the geometry. A finite element model was made to predict the frequency, based on geometry, density and elasticity matrix. After predicting the appropriate elastic constants, the RUS spectrum amplitude on different targets with different draw plug was studied. Experimental results from the contact pressure analysis was discussed. Theoretical study was completed to see the effect of radiation on mechanical properties of the material. After carefully studying the radiation effect on material, some recommendations can be made to use this technique properly inside a hot cell.

4.1 Conclusion

Experimentally detected frequency based on the quality factor is shown in Figure 3.1. Minimum frequency was detected around 250 kHz. Theoretically, below 250 kHz some modes existed, but due to the length and weight of the sample all these mode frequencies had undetectable responses. In RUS, a Demarest plot is usually used to measure the experimental Poisson's ratio. However, to generate a complete Demarest plot, it is necessary to experimentally detect first 20 modes. A

time-of-flight method can be handy in this situation to measure Poisson's ratio for an isotropic material. Even though the finite element method used in this study was highly time consuming, a simple mesh study was done to see the effect of the meshing on the eigen frequencies. A two pinducer system with a different holding mechanism was used to detect the frequencies below 250 kHz. But because of the size and shape of the sample the experiment was done in "surface to surface" manner. To extract all the frequencies below 300 kHz a study should be done to make a sophisticated detection system. To see the effect on the spectrum three different targets were made with three different plug sizes, which produced distinguishable responses.

4.2 Recommendations

Based on the result discussed above, a couple of recommendations can be made. The importance of sophisticated measurement system has already been established. Machining of the sample is very important, any non-uniformity will produce discrepancies in the frequency response. Before using RUS to measure radiation effects, some parameters should be considered. Dimensional change can happen after irradiation (Figure **??**). Before making any RUS measurement it is necessary to measure the dimension properly. Temperature has profound effect on the elastic constants. So cooling down of the irradiated material, and proper heat treatment might be necessary for the sample. An experiment can be designed to measure the contact resistance of the assembled targets. A numerical model of the assembled targets might help to understand the behavior of the RUS responses.

4.3 Future Work

Future work in extending RUS method should involve looking at the development of a quantitative measurement system for contact pressure between two cylinders. Creating a correlation between the thermal contact resistance and amplitude of the

target would help to mathematically explain the phenomena. This idea is based on the experimental results from target. To use RUS in radiation environment, inserting the whole setup in the hot cell is an important step. The transducer response in the radition field should be studied. Study of non-uniformity and anisotropy in the field of RUS may help in studying radiation damage with RUS.

Chapter 5

Acknowledgments

5.1 Thermal Contact Resistance

When two bodies come in contact, heat flows from the hotter to the colder body. A temperature difference is observed at the interface between the two surfaces in contact. The magnitude of the temperature drop is related to the *thermal contact resistance* between the contacting surfaces. Thermal contact resistance is an effect due to surface roughness causing a temperature drop across the interface. These surface irregularities creates intermittent points of contact and air gap in the interface. The heat transfer is actually governed by both the conduction through the contact spots and conduction or convection/radiation across the gaps.

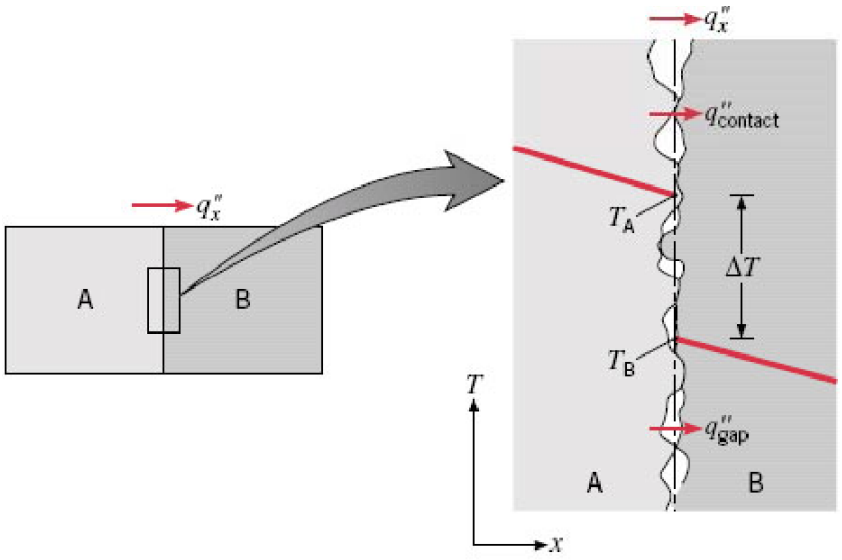

Figure 5.1: Temperature drop due to thermal contact resistance

$$q_x^{''} = q_{contact}^{''} + q_{gap}^{''} \tag{5.1}$$

Where $q_x^{''}$ is total heat transfer across the contacting surfaces. Figure 5.1 shows temperature drop across the contact surface[4]. Thermal contact resistance is a function of the temperature difference due to surface imperfection and the heat transfer rate. This relationship can be shown in the following way.

$$R = \frac{\Delta T}{q_x^{''}} \tag{5.2}$$

Where R is the thermal contact resistance and ΔT is the temperature difference across the interface of the two surfaces.

5.2 Contact Pressure

As discussed in the previous section heat transfer through the interfaces formed by the mechanical contact of two solids occurs in three forms: conduction through contacting spots, conduction through the gas-filled voids and radiation. In normal situations, radiation effects are small compared to the other two parameters. Another geometric parameter that controls the heat transfer through the contacting spots is the ratio of actual to apparent areas of contact. This ratio is called *contact pressure* which is determined by *relative contact pressure*. The relative contact pressure is defined as the ratio of applied pressure to the contact microhardness(P/H_c). This relative contact pressure also plays an important role in the thickness of the air gap between the contacting interfaces. The ratio P/H_c controls three geometric factors that control the heat transfer: contact spot density, mean contact spot radius, and separation distance of the mean planes of the two contacting surfaces [31]. Contact microhardenss, H_c, depends on several parameters: mean surface roughness, method of surface preparation and applied

pressure. An explicit relation was found in reference [31] for the relative contact pressure

$$\frac{P}{H_c} = \left[\frac{P}{(1.62 \times 10^6 \sigma/m)^{c_2}}\right]^{\frac{1}{1+.071c_2}} \tag{5.3}$$

Here σ is the RMS surface roughness and c_2 is the Vickers correlation coefficients.

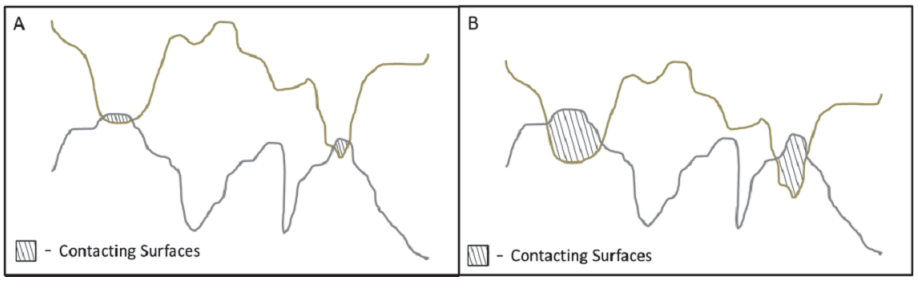

Figure 5.2: Magnified profile of two surfaces in contact with changing contact pressure(A)less contact pressure (B)higher contact pressure

Figure 5.2 shows the change of contacting surface based on the contact pressure. Consequently it will also change the thermal contact resistance. In the context of Molybdenum-99 targets contact pressure plays an important role in design [22], and choosing appropriate forming pressure. Reducing the contact resistance is one of the major challenges of designing the target. Low contact resistance will help to remove heat throughout the irradiation process which is necessary for the safety of the target. It is not possible to experimentally determine the actual contact pressure between the surfaces. For plastically deformed surfaces Yovanovich [20] proposed the following correlation for thermal contact conductance :

$$\frac{h_c \sigma}{k tan\theta} = 1.25 \left(\frac{P}{H_c}\right)^{0.95} \tag{5.4}$$

Here h_c is solid spot conductance, $tan\theta$ is the mean absolute slope for the surface profile and k is the harmonic mean conductivities of the two contacting surfaces.

5.3 Experiment

5.3.1 Target Assembly

This particular experiment was designed to investigate the effect of different contact pressures effect on the RUS spectrum. To characterize the contact pressure between two concentric cylinders, three different targets were made using three different draw plug sizes without any foil. Since three different plug sizes were used to make three different targets, the contact pressures are different in each target. The draw plug assembly procedure was used to make the targets (Figure 5.3). The draw plug target manufacturing method or drawing process uses a die and plug to mechanically expand the inner tube while holding the outer tube in steady. The two aluminum tubes cut to a specified length are pre-manufactured (with proper tolerance) so that inner tube can slide freely into the outer tube.

Once the tubes have been slid together, they are placed in a die that confines the outer tube in the drawing process. A hydraulically driven rod with a plug attached to the end is then forced through the inner tube. The size of the plug is important because it deforms the inner tube plastically, and thus reduces the gape between the two cylinders. Increasing the plug size will increase the deformation that occurs in the inner tube (aluminum) leading to an increase in contact pressure. Figure 5.3 shows the draw pug set up for target manufacturing.

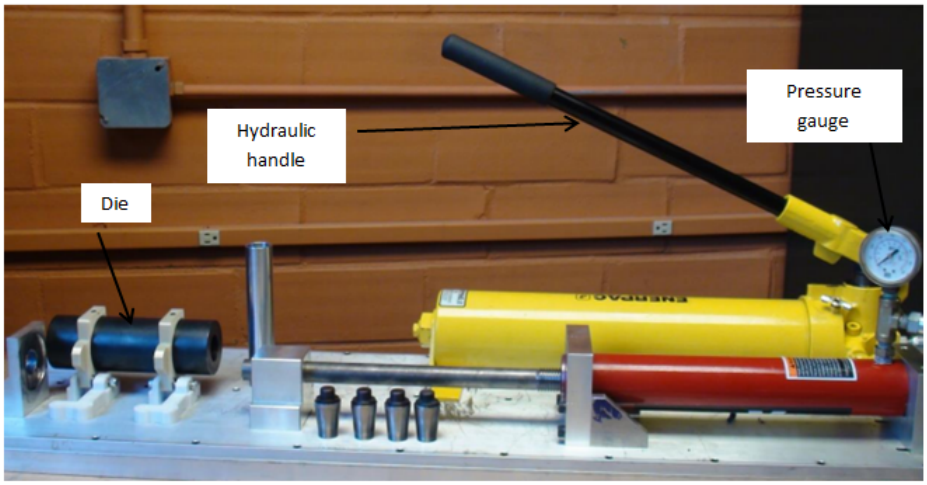

Figure 5.3: Draw plug Rig

As mentioned earlier, the inner tube deforms plastically as the plug is drawn though. The outer tube deforms elastically. During the manual process of drawing the plug through the inner tube, the formation (drawing) pressure was recorded. This is the required pressure to drive the plug through the target which is not an actual forming pressure, but it provides a qualitative idea about the deformation. Higher forming pressure means higher deformation.

Table 5.1: Weights of the three different targets

Draw plug ID	Plug Outer Diameter (m)	Tube Length (m)	Target Mass (g)
48	0.02662	0.161	61.470
49	0.02664	0.161	60.942
50	0.02667	0.161	61.213

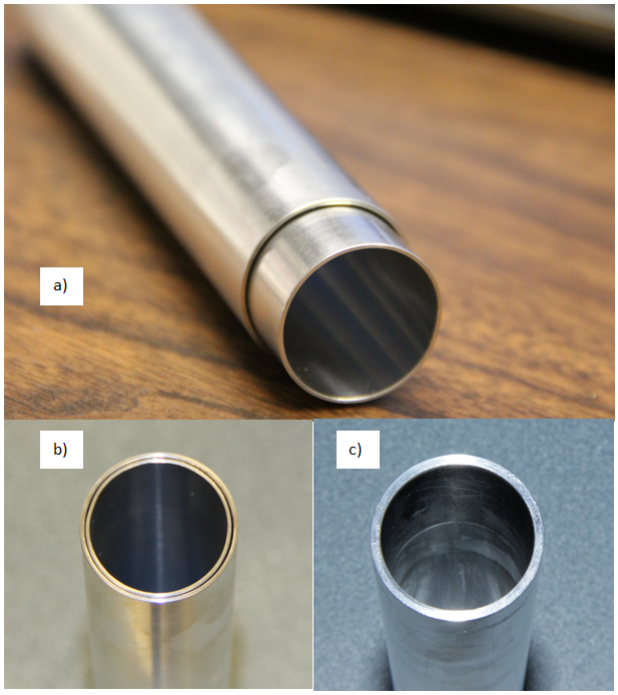

Figure 5.4: a)Inner and Outer tubes together b)Two concentric cylinders before deformation c)After assembling the target

Forming pressure for the two plugs (48 and 50) is shown in Figure 5.6. As can be seen from the plot that forming pressures are also different for different plugs along the distance of the target, but they have a similar trend. At the beginning of the process the required pressure is higher.

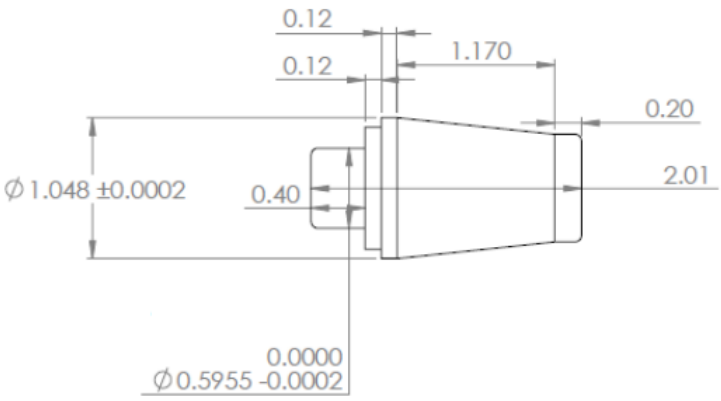

Figure 5.5: Dimensions(inches) of a draw plug(48)

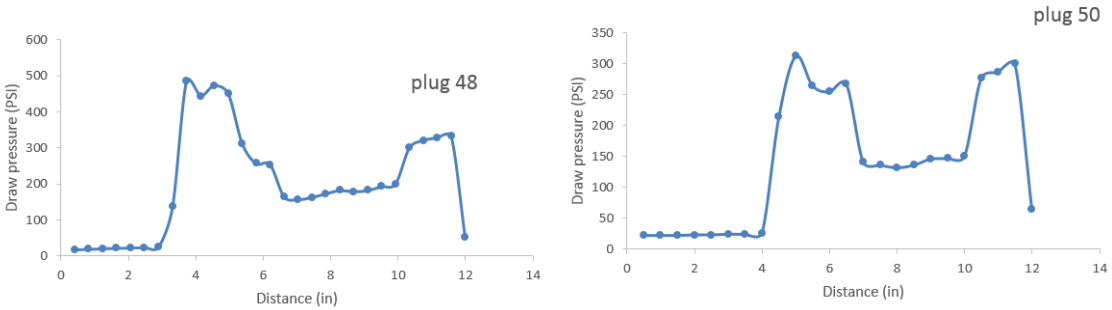

(a) plug 48 (b) plug 50

Figure 5.6: Plot of pressure during swagging using two different plug sizes

5.3.2 Results

The purpose of this experiment was to detect variations in RUS spectrum in different contact pressures which is related to thermal contact resistance. Since three different draw plugs were used (plug 48, 49 and 50), it is assumed that the targets have three different contact pressures. The outer diameter of the plugs are shown in Table 5.1.

To evaluate the RUS responses of the targets, the spectrum of the individual tube (inner and outer) is studied. The spectrum of the outer tube is shown in Figure 5.7. The inner tube also shows the same type of response (Figure 5.8). All three tubes show a similar pattern. At around 8.3×10^5 Hz there is a response around 0.9×10^{-4} volts. The amplitude of the peaks is considered for this experiment. Since the geometry is a hollow cylindrical and the mass is constant before and after making the target, the only variable will be the amplitude.

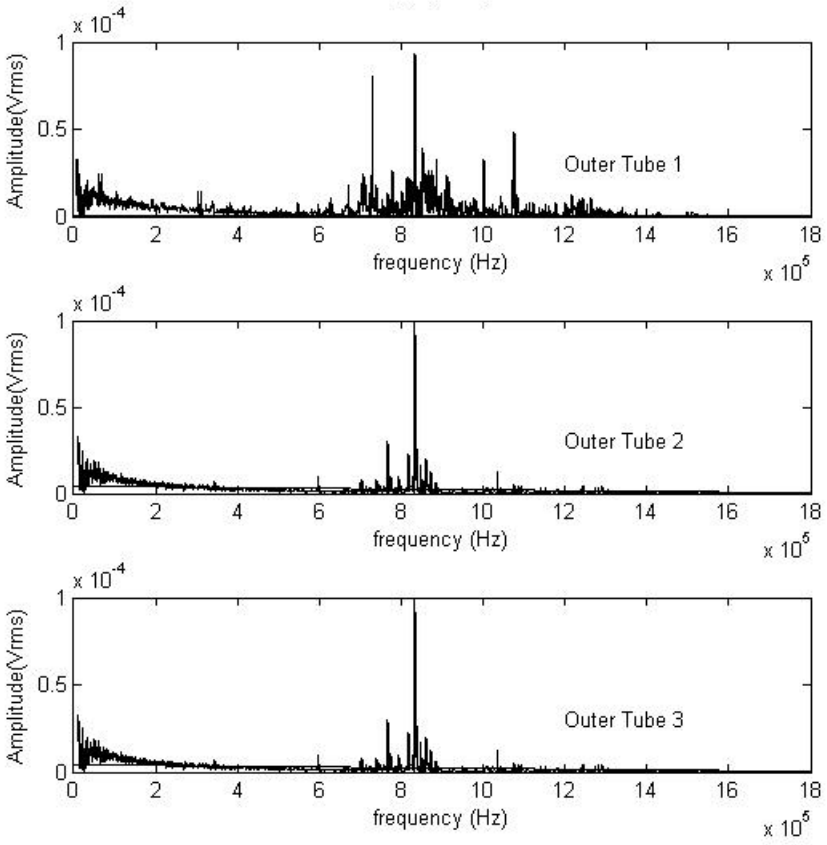

Figure 5.7: RUS spectrum of the outer tube

The diameter of the plug varies from 0.02662 m to 0.02667 m . These different plug sizes will exert different pressures in the inner tubes. As the plug size increases, it will cause more plastic deformation on the inner tube. Given the sizes of the plugs it is assumed that only the inner tube is plastically deformed [13]. Outer tube's deformation is elastic. Mass of the object plays an important role in response of the of the amplitude. The masses of the three different targets are in Table 5.1 .

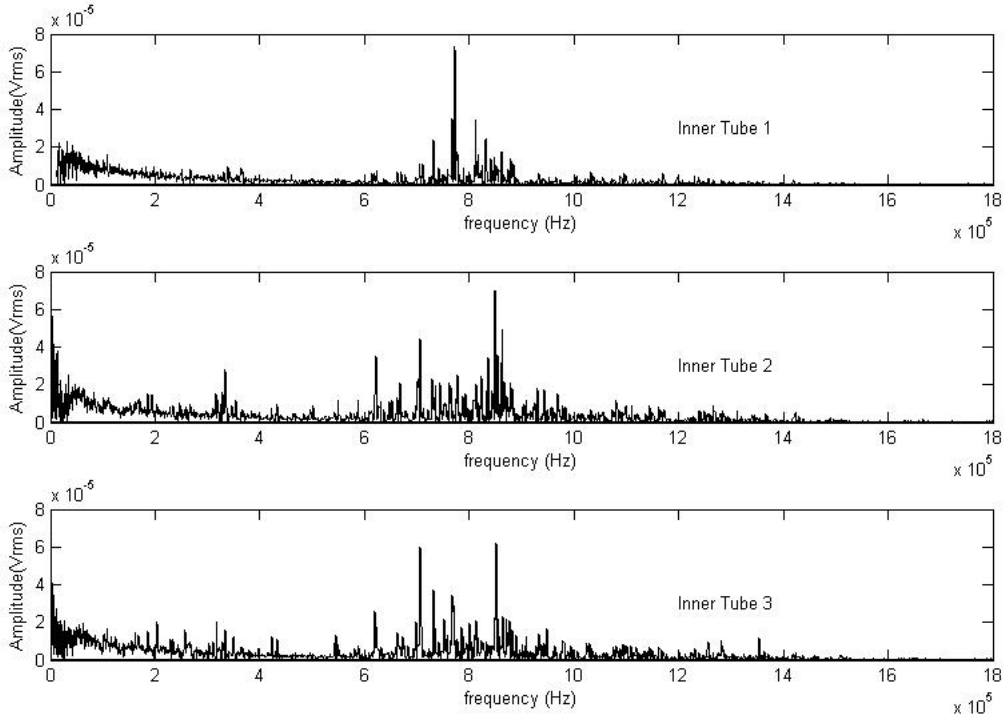

Figure 5.8: RUS spectrum of the inner tube

The experimental findings of the RUS of the three different assembled targets are shown in Figure 5.9.

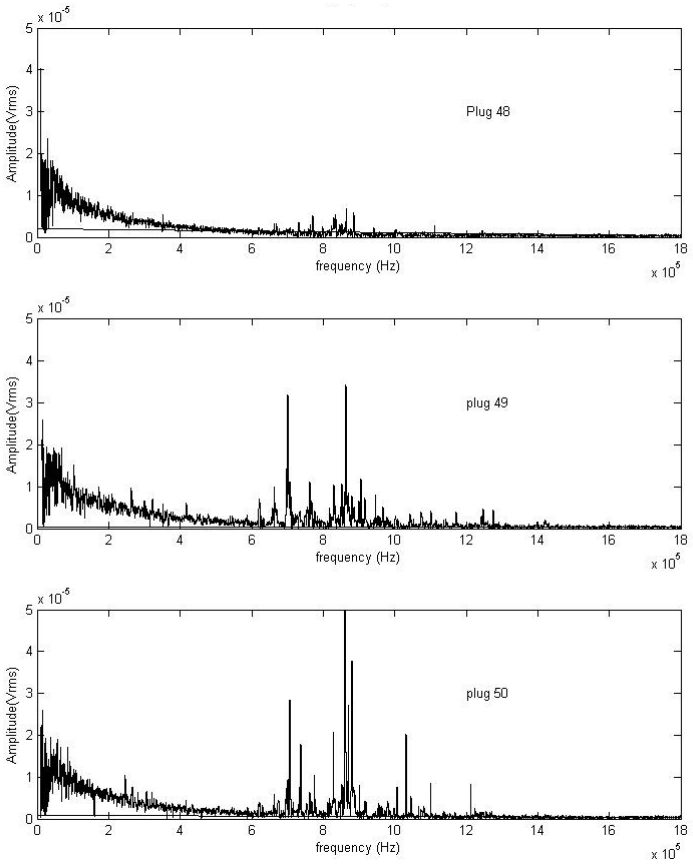

Figure 5.9: RUS spectrum of the targets

Figure 5.9 shows the RUS response for three different targets. The frequency range that we are interested in is 6.5 to 10 $\times$ Hz. In this frequency range the amplitudes vary significantly. The result can be summarized in Table 5.2.

Table 5.2: Highest amplitudes in the interested frequency zone

Draw plug size	frequency range $(\times 10^5)Hz$	Amplitude $(V_{rms} \times 10^{-5})volts$
48	6.5-9	1
49	6-10	3.5
50	6-10	5

The differences in the amplitudes of spectrum can be explained using the contact pressure between the two cylinders. Since the inner tube plastically deformed with three different radii, contact pressures are different in these targets. The RUS setup used to excite and measure the frequency spectrum is same as Figure **??**. As

the draw plug size increases the response amplitudes increases. From Figure **??**, only the outer tube is excited and the receiving transducers are receiving signals from the outer tube. Since the masses of these targets are almost the same (Table 5.1), the amplitude depends on the modes that are being produced. Since aluminum is used for both inner and outer tube, surface roughness does not change for the deformed targets. The only variable that can influence the response in RUS has to be *contact pressure* (Equation 5.4).

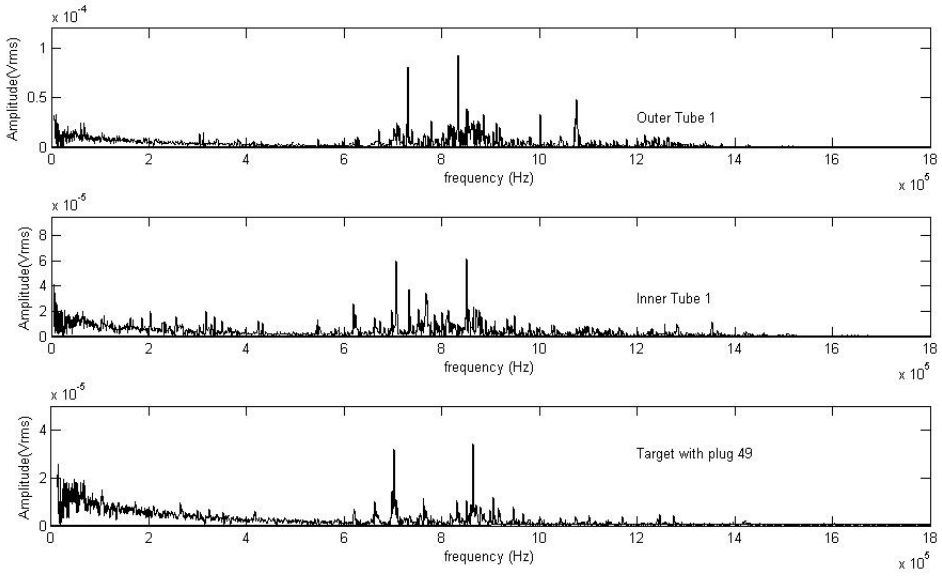

Figure 5.10: RUS spectra of outer tube, inner tube and one of the targets

Figure 5.10 shows that outer tube has a response around $1 \times 10^{-4}V$ and the inner is around $0.8 \times 10^{-4}V$. When they are pressed together with draw plug 49, the response reduced to around $0.4 \times 10^{-4}V$. All the individual tubes' (inner and outer) response were examined before they were deformed to a target.

Bibliography

[1] Orson L Anderson. *Equations of state of solids for geophysics and ceramic science*. Oxford University Press, 1995.

[2] Orson L Anderson et al. "Elastic properties of a micro-breccia, igneous rock and lunar fines from Apollo 11 mission". In: *Geochimica et Cosmochimica Acta Supplement* 1 (1970), p. 1959.

[3] Bertram Alexander Auld. *Acoustic fields and waves in solids*. Vol. 1. John Wiley and Sons, 1973.

[4] Theodore L Bergman, Frank P Incropera, and Adrienne S Lavine. *Fundamentals of heat and mass transfer*. John Wiley & Sons, 2011.

[5] *Colorado School of mines, Department of Physics*. `http://physics.mines.edu/about/downloads/software/mpl/main.pdf`. Accessed: 2014-03-13.

[6] Harold H Demarest Jr. "Cube-Resonance Method to Determine the Elastic Constants of Solids". In: *The Journal of the Acoustical Society of America* 49.3B (1971), pp. 768–775.

[7] DB Fraser and RC LeCraw. "Novel method of measuring elastic and anelastic properties of solids". In: *Review of Scientific Instruments* 35.9 (1964), pp. 1113–1115.

[8] Denos C Gazis. "Exact Analysis of the Plane-Strain Vibrations of Thick-Walled Hollow Cylinders". In: *The Journal of the Acoustical Society of America* 30.8 (1958), pp. 786–794.

[9] Denos C Gazis. "Three-Dimensional Investigation of the Propagation of Waves in Hollow Circular Cylinders. I. Analytical Foundation". In: *The journal of the Acoustical Society of America* 31.5 (1959), pp. 568–573.

[10] Richard Hallion. *Designers and test pilots*. Time Life Education, 1983.

[11] Paul Heyliger et al. "Elastic constants of isotropic cylinders using resonant ultrasound". In: *The Journal of the Acoustical Society of America* 94.3 (1993), pp. 1482–1487.

[12] R Hoppe. "Vibrationen eines Ringes in seiner Ebene." In: *Journal für die reine und angewandte Mathematik* 73 (1871), pp. 158–170.

[13] Annemarie Hoyer. "An Investigative Approach to Explore optimum assembly Process Design for Annular Targets Carrying LEU Foil". MA thesis. University of Missorui-Columbia, 2013.

[14] Tim Jaglinski and Yun-Che Wang. "On the use of hollow tube geometries for resonant ultrasound spectroscopy". In: *The Journal of the Acoustical Society of America* 129.4 (2011), pp. 1890–1898.

[15] Horace Lamb. "On the vibrations of an elastic sphere". In: *Proceedings of the London Mathematical Society* 1.1 (1881), pp. 189–212.

[16] Guangyan Li, GA Lamberton Jr, and JR Gladden. "Acoustic modes of finite length homogeneous and layered cylindrical shells: Single and multiwall carbon nanotubes". In: *Journal of Applied Physics* 104.3 (2008), p. 033524.

[17] RG Litwiller. *Resonant Ultrasound Spectroscopy and the Elastic Properties of Several Selected Materials*. 2000.

[18] Guoxing Liu and JD Maynard. "Measuring elastic constants of arbitrarily shaped samples using resonant ultrasound spectroscopy". In: *The Journal of the Acoustical Society of America* 131.3 (2012), pp. 2068–2078.

[19] Augustus Edward Hough Love. *A treatise on the mathematical theory of elasticity*. Cambridge University Press, 2013.

[20] Chakravarti V Madhusudana and CV Madhusudana. *Thermal contact conductance*. Springer, 1996.

[21] GD Mahan. "Oscillations of a thin hollow cylinder: carbon nanotubes". In: *Physical Review B* 65.23 (2002), p. 235402.

[22] Philip Franklin Makarewicz. "Thermal,Mechanical,Hydraulic Experimental Tools for Molybdenum-99 Production Target Analysis". MA thesis. University of Missouri-Columbia, 2013.

[23] Julian Maynard. "Resonant ultrasound spectroscopy". In: *Physics Today* 49.1 (2008), pp. 26–31.

[24] Albert Migliori and Timothy W Darling. "Resonant ultrasound spectroscopy for materials studies and non-destructive testing". In: *Ultrasonics* 34.2 (1996), pp. 473–476.

[25] Albert Migliori and John L Sarrao. *Resonant ultrasound spectroscopy: applications to physics, materials measurements, and nondestructive evaluation*. Wiley-Interscience, 1997.

[26] Ichiro Ohno. "Free vibration of a rectangular parallelepiped crystal and its application to determination of elastic constants of orthorhombic crystals." In: *Journal of Physics of the Earth* 24.4 (1976), pp. 355–379.

[27] Jiri Plesek, Radek Kolman, and Michal Landa. "Using finite element method for the determination of elastic moduli by resonant ultrasound spectroscopy". In: *The Journal of the Acoustical Society of America* 116.1 (2004), pp. 282–287.

[28] Lt Pochhammer. "Ueber die Fortpflanzungsgeschwindigkeiten kleiner Schwingungen in einem unbegrenzten isotropen Kreiscylinder." In: *Journal für die reine und angewandte Mathematik* 81 (1876), pp. 324–336.

[29] André Preumont. *Twelve lectures on structural dynamics*. Springer, 2013.

[30] Lord Rayleigh. "On the free vibrations of an infinite plate of homogeneous isotropic elastic matter". In: *Proceedings of the London Mathematical Society* 1.1 (1888), pp. 225–237.

[31] S Song and M Yovanovich. “Relative contact pressure-Dependence on surface roughness and Vickers microhardness”. In: *Journal of thermophysics and heat transfer* 2.1 (1988), pp. 43–47.

[32] William M Visscher et al. “On the normal modes of free vibration of inhomogeneous and anisotropic elastic objects”. In: *The Journal of the Acoustical Society of America* 90.4 (1991), pp. 2154–2162.

[33] Yun-Che Wang and Roderic S Lakes. “Resonant ultrasound spectroscopy in shear mode”. In: *Review of scientific instruments* 74.3 (2003), pp. 1371–1373.

[34] Brian J Zadler et al. “Resonant ultrasound spectroscopy: theory and application”. In: *Geophysical Journal International* 156.1 (2004), pp. 154–169.

[35] Brian Zadlert. “Properties of elastic materials using contacting and non-contacting acoustic spectrocopy”. PhD thesis. Colorado School of Mines, 2005.

Appendix A

XYZ Algorithm

```
clc
clear all
NN=input('Input the value of N');
%------next 13 lines assign an index IG to each basis function
C=zeros(3,3,3,3);
IG=0;
for I=1:3
    for L=1:NN+1
        for M=1:NN+1
            for N=1:NN+1
             if (L+M+N > NN+3), break, end
             IG=IG+1;
             IC(IG)=1;
             LB(IG)=1;
             MB(IG)=1;
             NB(IG)=1;

            end
        end
    end

end
rank=0.5*(NN+1)*(NN+2)*(NN+3);
NR=IG;
Gamma=zeros(rank,rank);
for IG=1:NR
     for JG=IG:NR
         I=IC(IG);
         J=IC(JG);
         LS=LB(IG)+LB(JG);
         MS=MB(IG)+MB(JG);
         NS=NB(IG)+NB(JG);

         Gamma(IG,JG)=C(I,1,J,1)*LB(IG)*LB(JG)*func(LS-2,MS,NS)+...
```

```
        C(I,2,J,2)*MB(IG)*MB(JG)*func(LS,MS-2,NS)+...
        C(I,3,J,3)*NB(IG)*NB(JG)*func(LS,MS,NS-2)+...
        C(I,1,J,2)*LB(IG)*MB(JG)+...
        C(I,2,J,1)*MB(IG)*LB(JG)*func(LS-1,MS-1,NS)+...
        C(I,1,J,3)*LB(IG)*NB(JG)+...
        C(I,3,J,1)*NB(IG)*LB(IG)*func(LS-1,MS,NS-1)+...
        C(I,2,J,3)*MB(JG)*NB(IG)+...
        C(I,3,J,2)*NB(IG)*MB(JG)*func(LS,MS-1,NS-1);
    Gamma(JG,IG)=Gamma(IG,JG);
  if(I==J) E(IG,IG)=func(LS,MS,NS) ;
    end
end
end


[vects vals]=eig(E\Gamma);
```